**Supplementary Information**

# Statistical benchmarking of bromide perovskite radiation detectors using industry-relevant performance metrics

Sergey V. Dayneko[1,2], Vishal Yeddu[1,2], Daniil Konorov[2], Kate Spicer[2], Nicholas Sandor[3], James Day[4], Antoine Pavesic Junior[2], Aleksandra I. Gracheva[1,2], Saeid Taherion[4], Magdalena Bazalova-Carter[5] and Makhsud I. Saidaminov[2,3,*]

[1]AY Sensors Inc., Victoria, British Columbia, Canada

[2]Department of Chemistry, University of Victoria, Victoria, British Columbia, Canada.

[3]Department of Electrical & Computer Engineering, University of Victoria, Victoria, British Columbia, Canada.

[4]Canadian Nuclear Laboratories, Chalk River, Ontario, Canada

[5]Department of Physics and Astronomy, University of Victoria, Victoria, BC V8W 2Y2, Canada

E-mail: msaidaminov@uvic.ca

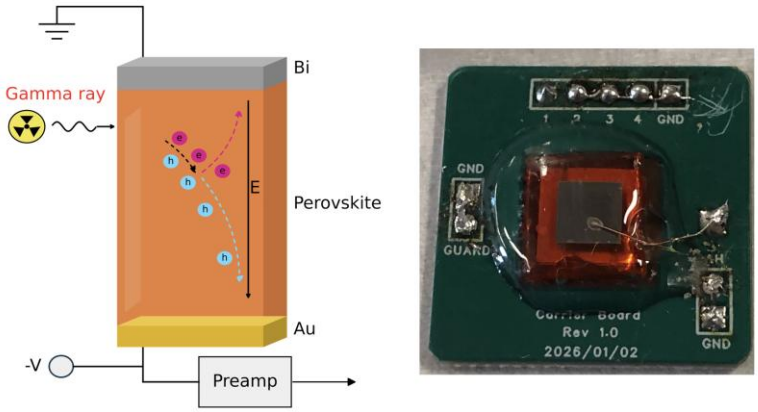


**Supplementary Fig. 1. Device architecture and implementation of bromide perovskite single-crystal detectors.** a) Schematic illustration of the detector structure and operating principle. Incident γ-rays generate electron–hole pairs within the perovskite crystal, which are separated and transported under an applied electric field (E) between asymmetric Bi/Au contacts. The induced signal is read out through a charge-sensitive preamplifier. b) Photograph of a fabricated device mounted on a custom-designed printed circuit board (PCB), showing the single-crystal perovskite, electrical contacts, guard ring configuration, and wire connections.

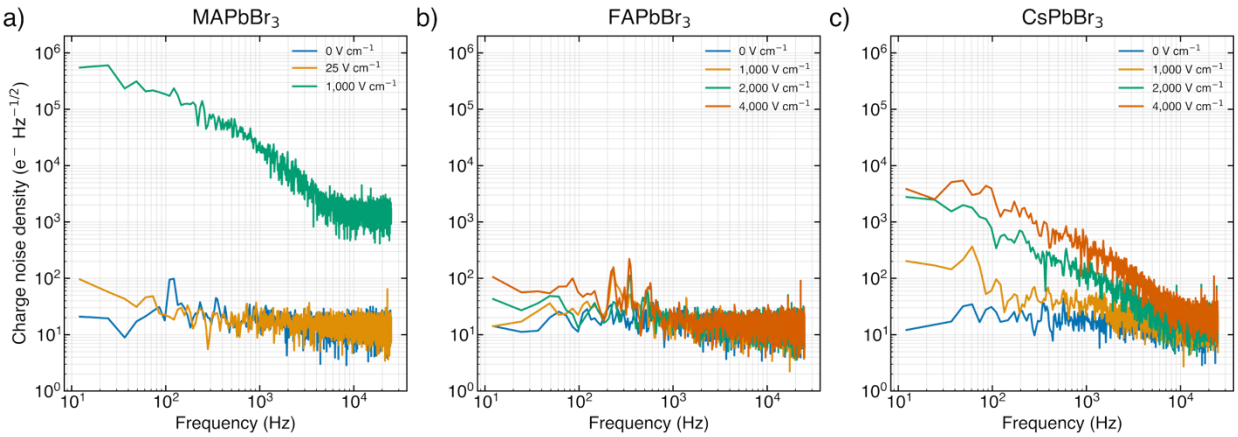


**Supplementary Fig. 2. Frequency-dependent charge-noise density in bromide perovskite single-crystal detectors**. Charge-noise spectral density measured under dark conditions for a) $MAPbBr_3$, b) $FAPbBr_3$, and c) $CsPbBr_3$ detectors at different electric fields.

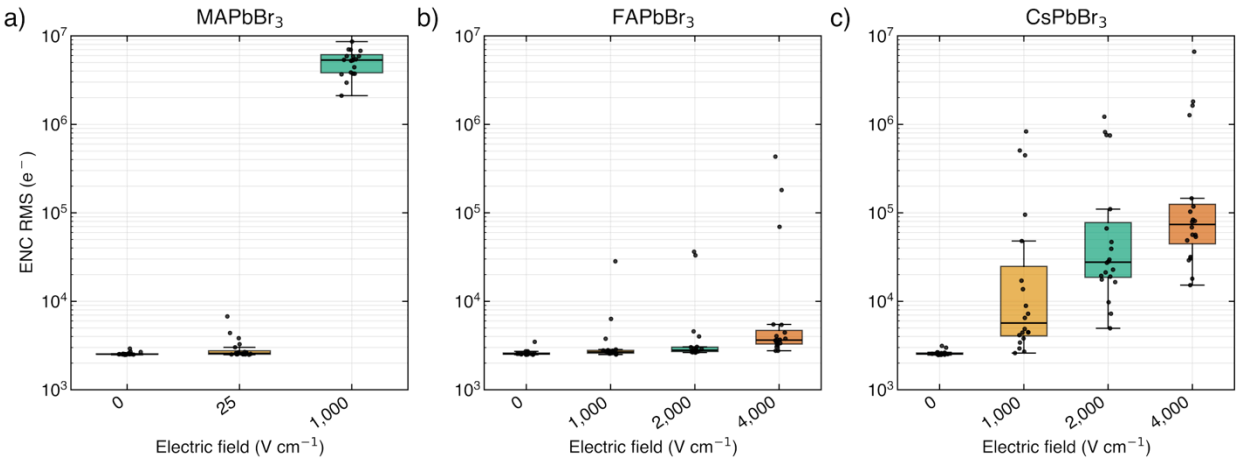


**Supplementary Fig. 3. Field-dependent *ENC* distributions in bromide perovskite single-crystal detectors**. Statistical distribution of *ENC* for a) $MAPbBr_3$, b) $FAPbBr_3$, and c) $CsPbBr_3$ detectors at different electric fields; each distribution was compiled from measurements of five independent devices with four pixels per device. The *ENC* values were calculated from the *RMS* baseline fluctuations under dark conditions and are presented on a logarithmic scale to highlight the strong field dependence of the electronic noise.

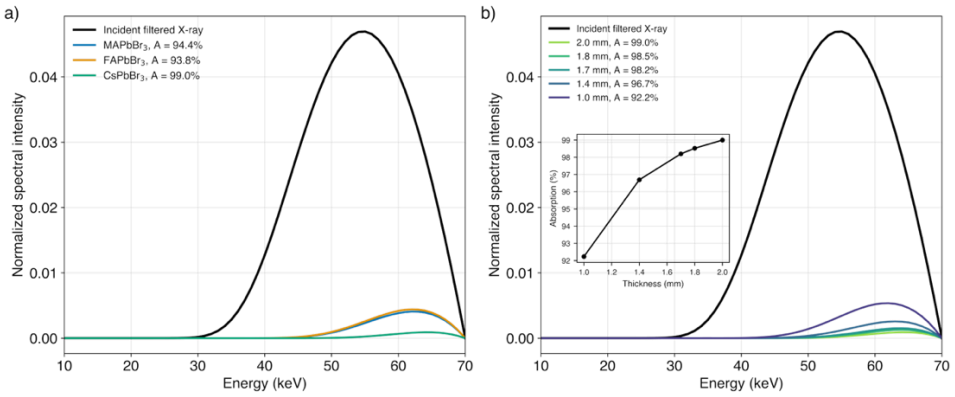


**Supplementary Fig. 4. Spectrum-weighted X-ray attenuation in bromide perovskite single crystals.** a) Filtered 70 kVp X-ray spectrum used in this study (black) and the transmitted spectra after passing through 2.0 mm thick $MAPbBr_3$, $FAPbBr_3$, and $CsPbBr_3$ single crystals. b) Thickness-dependent attenuation of $CsPbBr_3$ single crystals for thicknesses ranging from 1.0 to 2.0 mm, together with the incident filtered X-ray spectrum. The inset shows the corresponding spectrum-weighted absorption as a function of crystal thickness, demonstrating saturation above ~1.5 mm.

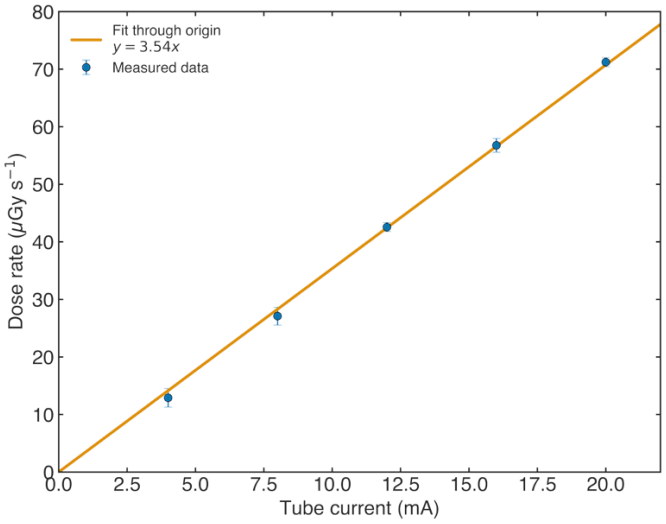


**Supplementary Fig. 5.** Current-to-dose-rate calibration curve for the filtered 70 kVp X-ray source used in this study. Dose rate was measured using a calibrated PTW TN23342W ionization chamber at 100 cm source-to-detector distance. The solid line shows the linear fit used for dose-rate conversion.

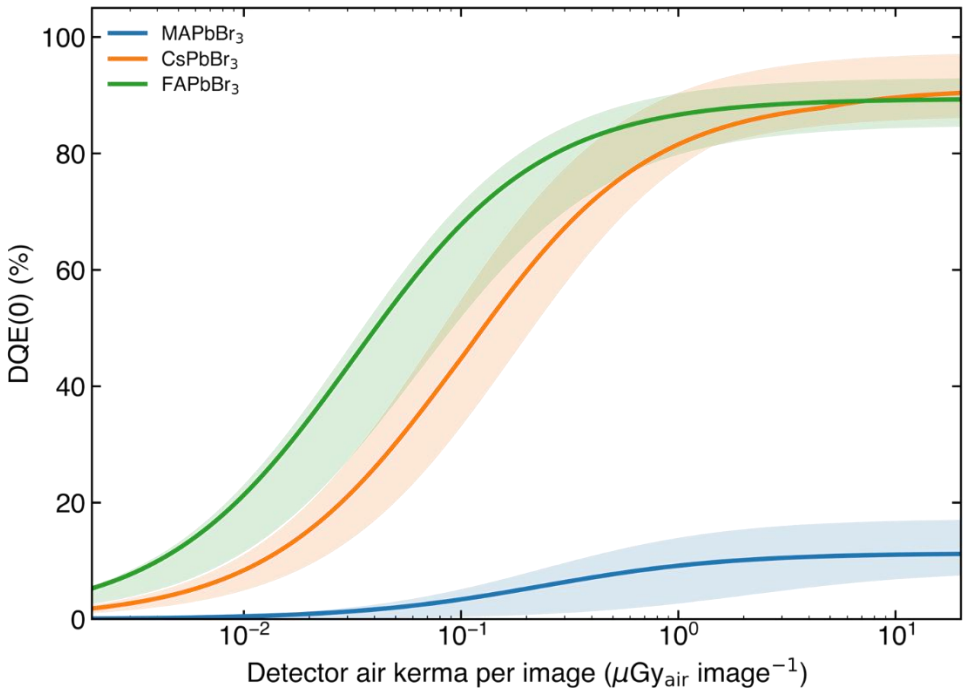


**Supplementary Fig. 6 Comparative *DQE(0)* performance at 20ms integration time.** Median zero-frequency detective quantum efficiency, DQE(0), as a function of detector air kerma per image (20 ms integration time) calculated using experimentally measured mobility–lifetime (μτ) products, detector thicknesses, spectrum-weighted X-ray absorption, and equivalent noise charge (ENC) values for $MAPbBr_3$, $CsPbBr_3$, and $FAPbBr_3$ detectors. The integration time corresponds to a frame rate of 50 frames $s^{-1}$, representative of dynamic fluoroscopy and photon-counting imaging.

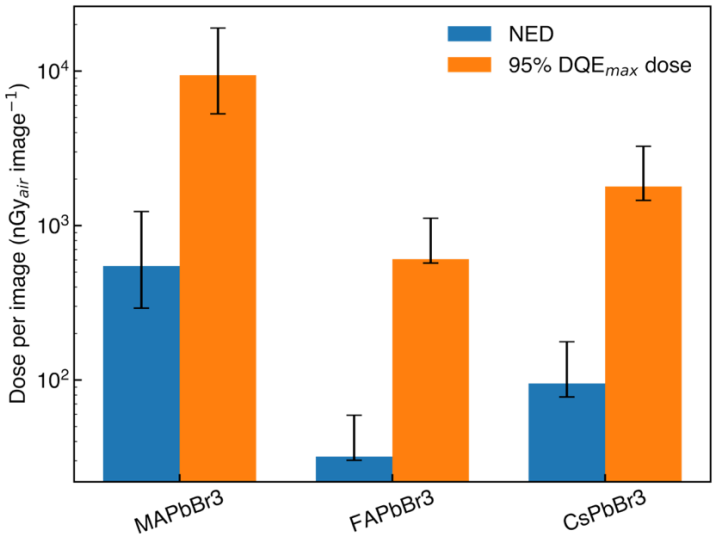


**Supplementary Fig. 7. Noise-equivalent dose (*NED*) and dose rate required to achieve near-saturated *DQE* performance for bromide perovskite single-crystal detectors.** Mean *NED* and dose rate required to reach 95% of the maximum simulated *DQE(0)* for $MAPbBr_3$, $FAPbBr_3$, and $CsPbBr_3$ devices, extracted from device-by-device *DQE* evaluation using experimentally measured $\mu\tau$ products and *ENC* values. Error bars represent the standard deviation across individual devices.

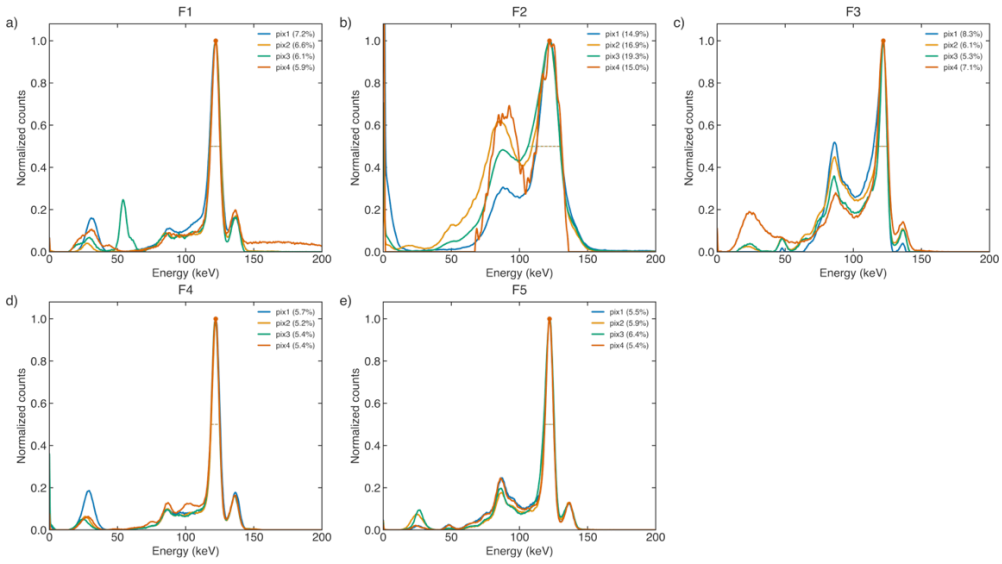


**Supplementary Fig. 8. Pixel-to-pixel *γ*-ray spectroscopy response of $FAPbBr_3$ single-crystal detectors under $^{57}Co$ irradiation**. Normalized *γ*-ray spectra recorded from the four individual pixels of $FAPbBr_3$ devices a) F1, b) F2, c) F3, d) F4 and e) F5. The values in parentheses indicate the energy resolution (FWHM at 122 keV) obtained for each pixel at electric field of 4,000 V $cm^{-1}$.

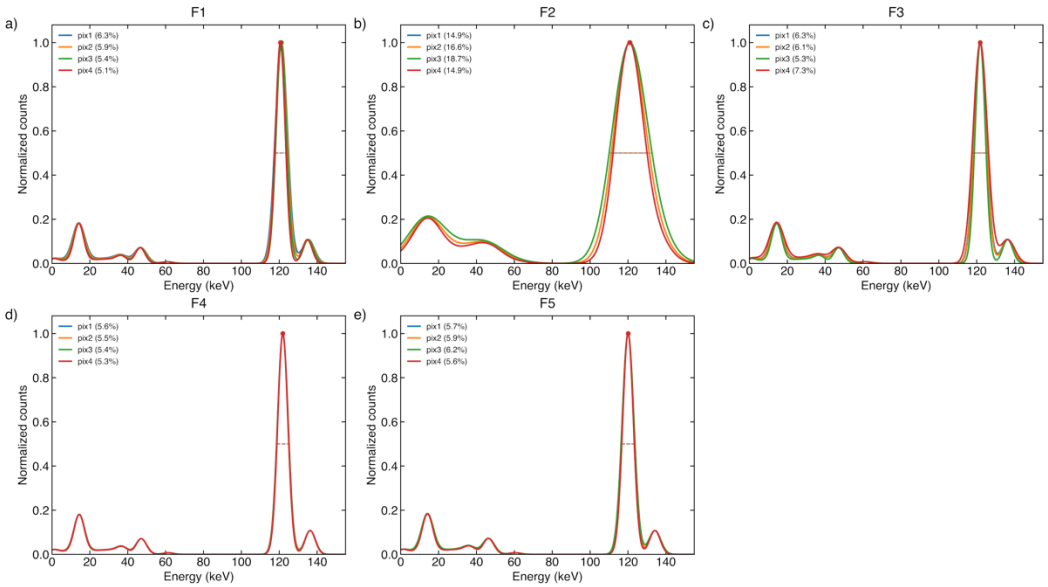


**Supplementary Fig. 9 Validation of the Monte Carlo charge-transport model for $FAPbBr_3$ detectors.** Detector-specific Monte Carlo simulations of $^{57}Co$ γ-ray spectra for all 20 $FAPbBr_3$ detector pixels using experimentally measured detector parameters. Agreement between the simulated spectra and the corresponding experimental spectra (Fig. 5 and Supplementary Fig. 8) validates the model before it is used to investigate detector performance with reduced electronic noise representative of advanced ASIC and CMOS readout electronics (Supplementary Fig. 10).

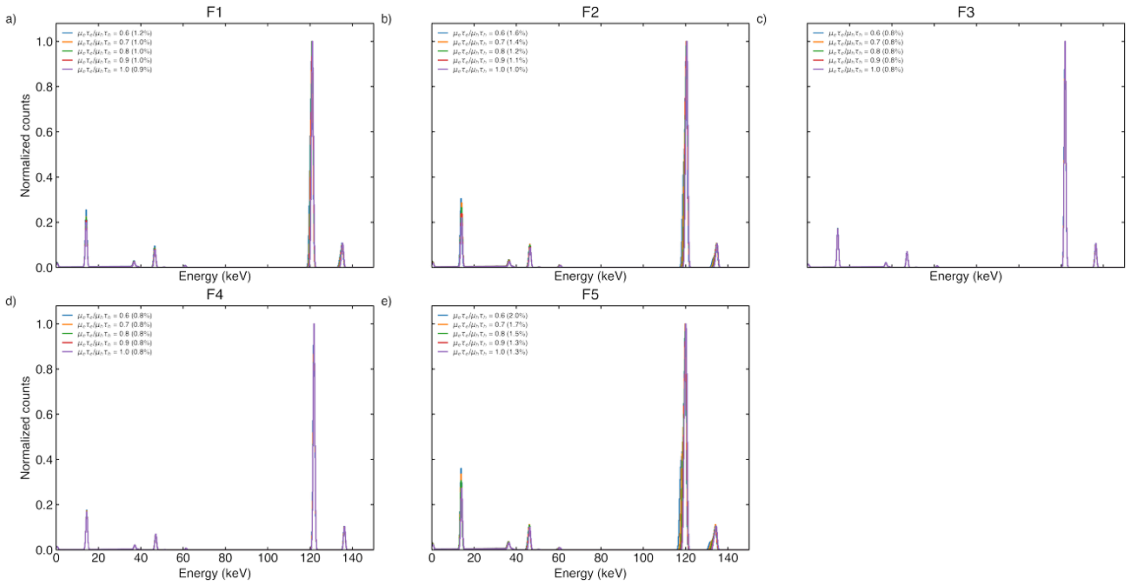


**Supplementary Fig. 10 Predicted γ-ray spectroscopy performance of $FAPbBr_3$ detectors with low-noise readout electronics.** Monte Carlo simulated $^{57}Co$ γ-ray spectra for all 20 $FAPbBr_3$ detector pixels using the experimentally measured detector thicknesses, mobility-lifetime products, operating electric fields and energy calibrations. The equivalent noise charge was reduced to 75 $e^-$ RMS, representative of state-of -art low-noise ASIC/CMOS front-end electronics, while all detector parameters were otherwise kept identical to the experimentally measured values. The simulations predict substantial narrowing of the 122.1 keV photopeak and consistent resolution of the 136.5 keV photopeak across all detector pixels, demonstrating that the intrinsic spectroscopic performance of $FAPbBr_3$ is presently limited primarily by electronic readout noise rather than by charge transport.

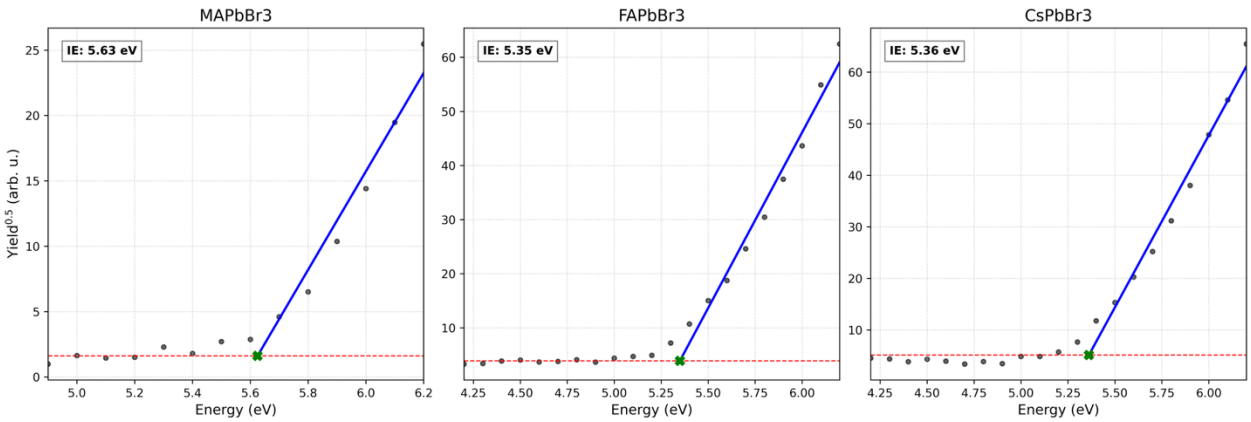


**Supplementary Fig. 11. Ionization energy (*IE*) for bromide perovskite single crystals measured by photoemission yield spectroscopy in air (PYSA).** Energy-dependent charge-yield analysis used to estimate the ionization energy (*IE*) for a) $MAPbBr_3$, b) $FAPbBr_3$, and c) $CsPbBr_3$ single crystals. The linear extrapolation of the high-energy region to zero charge yield was used to determine the effective ionization energy for each composition.

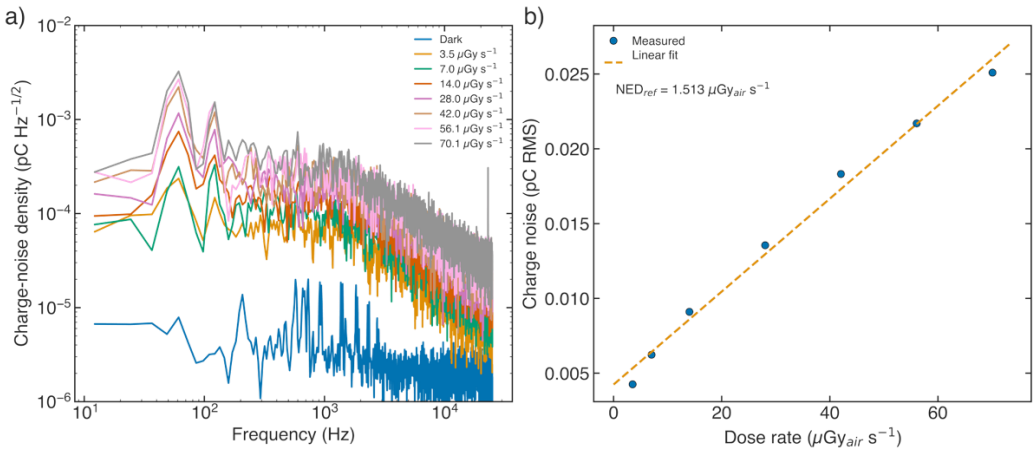


**Supplementary Fig. 12. Frequency-dependent electronic-noise characterization and extraction of the noise-equivalent dose (NED).** a) Frequency-dependent charge-noise spectral density measured for the perovskite detector under dark conditions and under X-ray irradiation at different dose rates at 1,000 V cm$^{-1}$. b) Root-mean-square (RMS) charge noise as a function of X-ray dose rate. Linear fitting of the noise–dose dependence was used to extract the reference noise-equivalent dose rate, yielding $NED_{ref}$ = 1.513 μGy$_{air}$ s$^{-1}$.

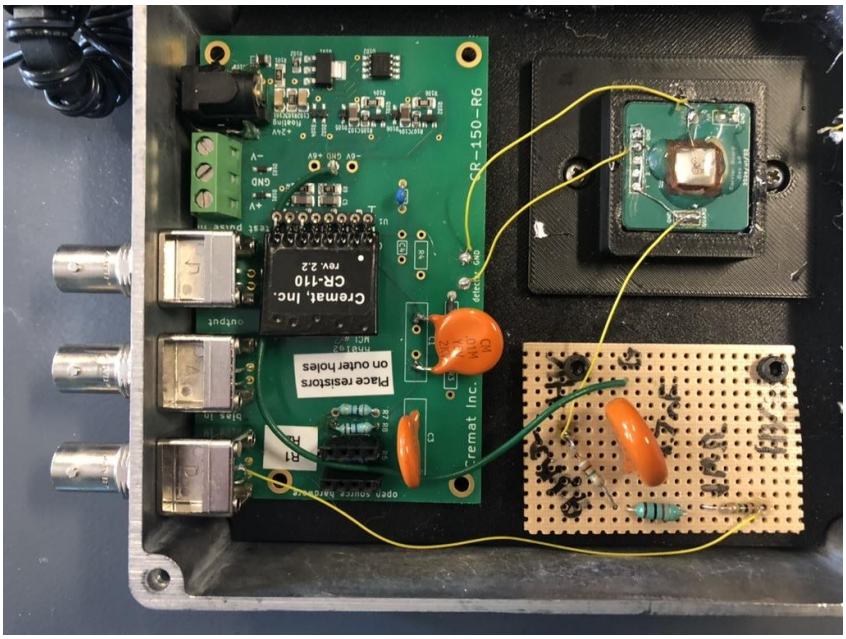


**Supplementary Fig. 13. Readout assembly for photon-counting γ-ray spectroscopy.** Photograph of the experimental readout configuration used for γ-ray spectroscopy measurements. A CR-110-R2.2 charge-sensitive preamplifier (Cremat Inc.) was installed on a modified CR-150-R6 evaluation board (Cremat Inc.). The detector carrier board is shown at the top right. The preamplifier output was connected to a CAEN DT5780M multichannel analyzer for pulse-height acquisition.

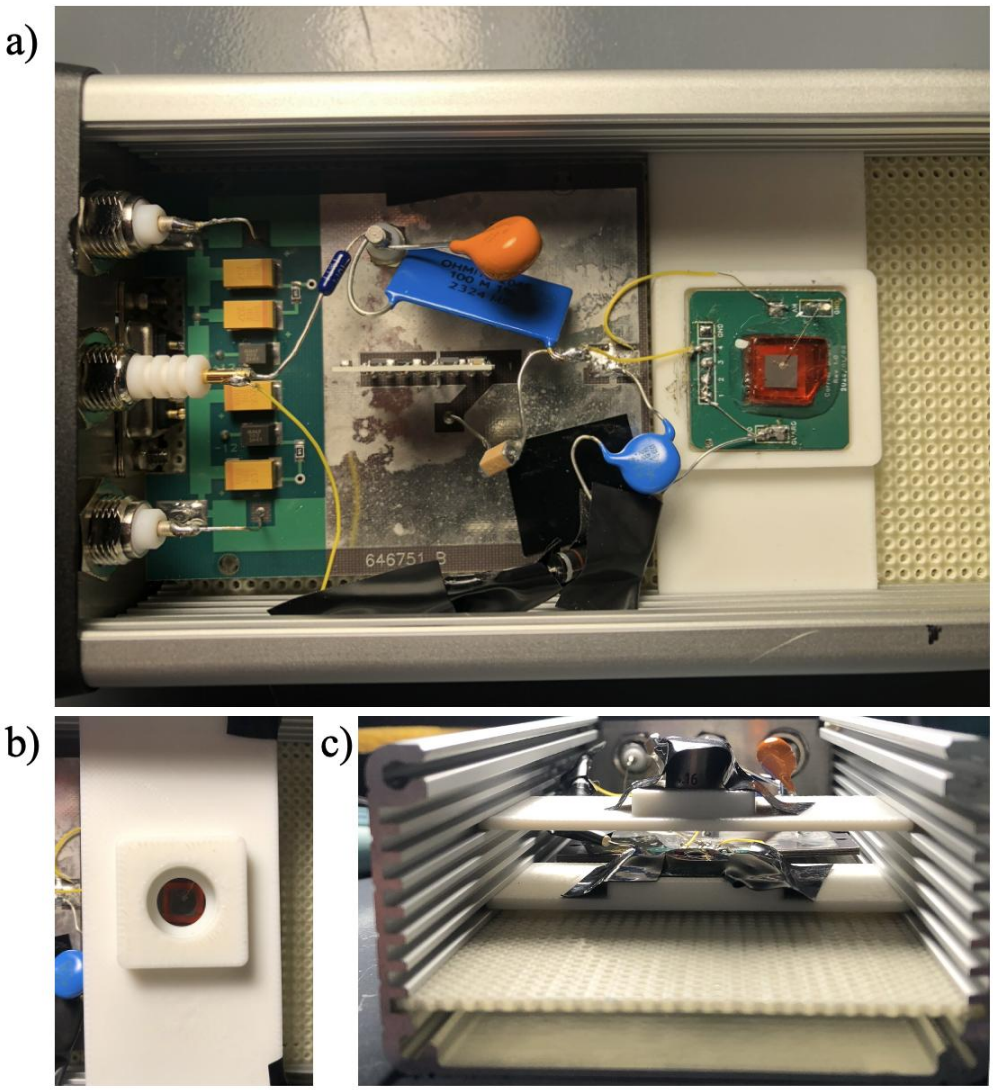


**Supplementary Fig. 14. Experimental γ-ray spectroscopy setup employing the EV550 low-noise charge-sensitive preamplifier (Kromek Ltd., UK)**. a) Internal view of the detector assembly showing the perovskite detector mounted on a carrier board and connected to the EV550 charge-sensitive preamplifier through a short low-capacitance input connection. b) Detector holder with a circular aperture exposing the detector top contact to the incident γ-ray beam. c) Side view of the measurement geometry, showing the sealed γ-ray source positioned directly above the detector along the detector normal during pulse-height spectroscopy measurements.